PTEP

Prog. Theor. Exp. Phys. **2020**, 073B07 (15 pages)
DOI: 10.1093/ptep/ptaa087

The HAL QCD potential in the $I = 1$ $\pi\pi$ system with the ρ meson bound state

Yutaro Akahoshi[1,2,*], Sinya Aoki[1,2], Tatsumi Aoyama[3,2], Takumi Doi[2,4], Takaya Miyamoto[2], and Kenji Sasaki[1,2]

[1]*Center for Gravitational Physics, Yukawa Institute for Theoretical Physics, Kyoto University, Kyoto 606-8502, Japan*
[2]*RIKEN Nishina Center (RNC), Saitama 351-0198, Japan*
[3]*Institute of Particle and Nuclear Studies, High Energy Accelerator Research Organization (KEK), Tsukuba, Ibaraki 305-0801, Japan*
[4]*RIKEN Interdisciplinary Theroretical and Mathematical Sciences Program (iTHEMS), Saitama 351-0198, Japan*
*E-mail: yutaro.akahoshi@yukawa.kyoto-u.ac.jp

Received April 6, 2020; Revised May 21, 2020; Accepted May 25, 2020; Published July 11, 2020

We investigate the HAL QCD potential in $I = 1$ $\pi\pi$ scattering using the hybrid method for all-to-all propagators, in which a propagator is approximated by low eigenmodes, and the remaining high-eigenmode part is stochastically estimated. To verify the applicability of the hybrid method to systems containing quark creation/annihilation contributions such as the ρ meson, we calculate the $I = 1$ $\pi\pi$ potential with the $(2 + 1)$-flavor gauge configurations on a $16^3 \times 32$ lattice with lattice spacing $a \approx 0.12$ fm and $(m_\pi, m_\rho) \approx (870, 1230)$ MeV, in which the ρ meson appears as a deeply bound state. While we find that the naive stochastic evaluations for quark creation/annihilation contributions lead to extremely large statistical fluctuations, additional noise reduction methods enable us to obtain a sufficiently precise potential, which shows a strong attractive force. We also confirm that the binding energy and $k^3 \cot\delta$ obtained from our potential are roughly consistent with an existing ρ meson bound state, within the large systematic error associated with our calculation, whose possible origin is also discussed.

Subject Index B64

1. Introduction

One of the most challenging issues in particle and nuclear physics is to understand hadronic resonances in terms of the fundamental theory of quarks and gluons, quantum chromodynamics (QCD). To achieve this goal, two methods for studying hadron–hadron interactions non-perturbatively in lattice QCD have been employed so far: Lüscher's finite-volume method [1–3] and the HAL QCD method [4–7]. Lüscher's finite-volume method enables us to calculate scattering phase shifts directly from finite-volume energy spectra. Pole structures of bound states and resonances can be addressed by the analytic continuation of the S-matrix into the complex energy region, which, however, would require some ansatz for the structure of the S-matrix, in particular for coupled channel systems. Several mesonic resonances, such as the ρ meson, have been studied in lattice QCD by this method [8,9]; see also Ref. [10] and the references therein.

In the HAL QCD method, on the other hand, energy-independent but non-local potentials of hadron interactions are constructed from the Nambu–Bethe–Salpeter (NBS) wave function calculated in lattice QCD, from which physical observables are extracted afterward. This method has a unique advantage for understanding hadronic resonances from first principles. In this method, once the

Funded by SCOAP[3]

potential is obtained, one can directly address the pole structure of the S-matrix without any additional model-dependent ansatz. The extension to coupled channel systems, which are often essential to understanding resonances, can be achieved in a straightforward manner [11]. Another strength of this method is that the signal of the potential can be extracted not only from the ground state but also from excited states, which is crucial for reliable calculations for baryon–baryon systems [7,12]. Various interesting results have been reported using this method, for example the identification of the $Z_c(3900)$ as the threshold cusp effect [13,14], and predictions on the existence of $\Omega\Omega$ and $N\Omega$ dibaryons at the physical point [15,16].

At present, however, studies of resonances with the HAL QCD method are restricted due to difficulty in treating all-to-all propagators with reasonable numerical cost and sufficient precision. In our previous attempts [17,18], we utilized the LapH method [19] to treat all-to-all propagators, and it was revealed that the LapH smearing on the sink operator enhances the non-locality of the potential, so that the leading-order approximation in the derivative expansion for the potential becomes insufficient. To establish a more suitable method for all-to-all propagators, we have recently applied the hybrid method [20], which treats all-to-all propagators with a low-eigenmode approximation plus the stochastic estimation for the remaining high modes, to the HAL QCD method [21]. In contrast to the LapH method, the hybrid method can maintain the locality of quark operators since it contains full information of the eigenmodes of the Dirac operator. In Ref. [21], we studied $I = 2$ $\pi\pi$ S-wave scattering with the hybrid method, and we confirmed that the combination of the HAL QCD method and the hybrid method gave us reliable results with better convergence of the derivative expansion, as long as appropriate choices of parameters for the hybrid method have been made.

In this paper we apply the hybrid method to the $I = 1$ $\pi\pi$ system and study the ρ meson. Since all-to-all propagators are mandatory to calculate quark creation/annihilation contributions, this is the best benchmark system to verify the applicability of the hybrid method. We calculate the potential on the gauge configurations at $(m_\pi, m_\rho) \approx (870, 1230)$ MeV, in which the ρ meson is not a resonance but a deeply bound state. It is revealed that stochastic estimations in the hybrid method for quark creation/annihilation contributions greatly enhance the statistical fluctuations of the HAL QCD potential, and therefore we require some additional noise reductions to obtain a sufficiently precise potential. As a consistency check, we calculate the binding energy and $k^3 \cot\delta$ from the resultant potential, and confirm that a deeply bound ρ state is reproduced within a somewhat large systematic error.

This paper is organized as follows. In Sect. 2 we briefly explain the HAL QCD method and the hybrid method. Details of the simulations in this study are given in Sect. 3. Our main result, the potential of the $I = 1$ $\pi\pi$ system, is presented in Sect. 4. We also discuss physical observables computed by the potential and the origin of their systematic uncertainty here. Our conclusion and the future outlook are given in Sect. 5.

2. Method

2.1. HAL QCD method

The fundamental quantity in the HAL QCD method is the NBS wave function, which is defined for the $I = 1$ two-pion system as

$$\psi_W(\mathbf{r}, \Delta t) = \langle 0|(\pi\pi)_{I=1,I_z=0}(\mathbf{r}, 0, \Delta t)|\pi\pi; I = 1, I_z = 0, \mathbf{k}\rangle, \tag{1}$$

where $|\pi\pi; I = 1, I_z = 0, \mathbf{k}\rangle$ is an asymptotic state for the elastic $I = 1$ $\pi\pi$ system in the center-of-mass frame with relative momentum $\mathbf{k}$, total energy $W = 2\sqrt{m_\pi^2 + k^2}$, and $k = |\mathbf{k}|$. The operator

$(\pi\pi)_{I=1,I_z=0}(\mathbf{r},t,\Delta t)$ is a local two-pion operator projected to the $I=1, I_z=0$ channel, explicitly given by

$$(\pi\pi)_{I=1,I_z=0}(\mathbf{r},t,\Delta t) = \frac{1}{\sqrt{2}}\sum_{\mathbf{x}}\{\pi^+(\mathbf{r}+\mathbf{x},t+\Delta t)\pi^-(\mathbf{x},t) - \pi^-(\mathbf{r}+\mathbf{x},t+\Delta t)\pi^+(\mathbf{x},t)\}, \quad (2)$$

where $\pi^+(\mathbf{x},t)$ ($\pi^-(\mathbf{x},t)$) is the positively (negatively) charged pion operator defined as $\pi^+(\mathbf{x},t) = \bar{d}(\mathbf{x},t)\gamma_5 u(\mathbf{x},t)$ ($\pi^-(\mathbf{x},t) = \bar{u}(\mathbf{x},t)\gamma_5 d(\mathbf{x},t)$) with up and down quark fields $u(\mathbf{x},t)$ and $d(\mathbf{x},t)$.

The above definition of the NBS wave function is more general than the equal-time ($\Delta t = 0$) NBS wave function conventionally employed in the HAL QCD method, where two sink hadron operators are put on the same time slice. In general, the HAL QCD potential depends on the choice of hadron operators in the definition of the NBS wave function; we call this the "scheme" dependence of the potential [17,22]. The potential derived from the NBS wave function with $\Delta t \neq 0$ belongs to the same scheme as the conventional equal-time scheme if we take $\Delta t \to 0$ in the continuum limit, while it belongs to a different scheme if we keep physical Δt finite in the continuum limit. Since the calculations in this study are performed only at one lattice spacing, we consider the results from $\Delta t = 0$ and $\Delta t \neq 0$ as those in two different schemes between which the discretization artifact appears differently.

While the potentials are scheme dependent, physical quantities such as phase shifts and binding energies, of course, do not depend on the scheme (up to the discretization errors). On can even take advantage of this arbitrariness by choosing a better scheme so that statistical/systematic errors are minimized. As discussed later, the main reason why we introduce the scheme with non-zero Δt is to reduce statistical fluctuations of the potential for the $I=1$ $\pi\pi$ system, which are caused by stochastic estimations for all-to-all quark propagators in the hybrid method.

As discussed in Refs. [5,23] for the case of the $\Delta t = 0$ scheme, we can show that the radial part of the lth partial component in the NBS wave function with the non-zero Δt scheme behaves at large $r = |\mathbf{r}|$ as

$$\psi_W^l(r,\Delta t) \approx A_l(\Delta t,\mathbf{k})e^{i\delta_l}\frac{\sin(kr - l\pi/2 + \delta_l(k))}{kr}, \quad (3)$$

where $A_l(\Delta t,\mathbf{k})$ is an overall factor and $\delta_l(k)$ is the scattering phase shift, which is equal to the phase of the S-matrix implied by its unitarity. By using this behavior, we can construct an energy-independent but non-local potential through the Schrödinger-type equation as

$$\frac{1}{2\mu}(\nabla^2 + k^2)\psi_W(\mathbf{r},\Delta t) = \int d^3\mathbf{r}'\, U_{\Delta t}(\mathbf{r},\mathbf{r}')\psi_W(\mathbf{r}',\Delta t), \quad (4)$$

where $\mu = m_\pi/2$ is a reduced mass of two pions, and a subscript Δt of U represents the scheme for the potential. In practice, the non-locality of the potential is treated by the derivative expansion as

$$U_{\Delta t}(\mathbf{r},\mathbf{r}') = \left(V_{\Delta t}^{\rm LO}(r) + V_{\Delta t}^{\rm NLO}(r)\nabla^2 + \mathcal{O}(\nabla^4)\right)\delta(\mathbf{r}-\mathbf{r}'). \quad (5)$$

The normalized $\pi\pi$ correlation function, numerically calculable in lattice QCD, is related to the NBS wave functions as

$$R(\mathbf{r},t,\Delta t) \equiv \frac{F(\mathbf{r},t,\Delta t)}{C(t)^2} \approx \sum_n B_n\psi_{W_n}(\mathbf{r},\Delta t)e^{-(W_n-2m_\pi)t} + \cdots, \quad (6)$$

where W_n and B_n are the energy and overlap factor of the nth excited elastic state, and the ellipsis indicates inelastic contributions. Here, $C(t)$ and $F(\mathbf{r}, t, \Delta t)$ are π and $\pi\pi$ correlation functions defined by

$$C(t) = \sum_{\mathbf{x},\mathbf{y},t_0} \langle \pi^-(\mathbf{x}, t + t_0)\pi^+(\mathbf{y}, t_0)\rangle, \tag{7}$$

$$F(\mathbf{r}, t, \Delta t) = \sum_{t_0} \langle (\pi\pi)_{I=1,I_z=0}(\mathbf{r}, t + t_0, \Delta t)\mathcal{J}^{T_1^-}_{I=1,I_z=0}(t_0)\rangle, \tag{8}$$

where $\mathcal{J}^{T_1^-}_{I=1,I_z=0}(t_0)$ is a source operator which creates $I = 1$ and $I_z = 0$ $\pi\pi$ scattering states in the T_1^- representation. Among several choices for the source operator, we take a ρ-type source operator in our study, given by

$$\mathcal{J}^{T_1^-}_{\rho;I=1,I_z=0}(t_0) = \sum_{\mathbf{x}} \bar{\rho}^0_3(\mathbf{x}, t), \tag{9}$$

where ρ^0_i is the neutral ρ meson operator, $\rho^0_i = \bar{u}\gamma_i u - \bar{d}\gamma_i d$. Since this source operator strongly overlaps with the ρ meson state, we expect that the truncation error of the derivative expansion in the effective leading-order analysis is suppressed around the mass of the ρ meson.

The normalized correlation function $R(\mathbf{r}, t, \Delta t)$ satisfies [7]

$$\left[\frac{\nabla^2}{m_\pi} - \frac{\partial}{\partial t} + \frac{1}{4m_\pi}\frac{\partial^2}{\partial t^2}\right] R(\mathbf{r}, t, \Delta t) = \int d^3\mathbf{r}' U_{\Delta t}(\mathbf{r}, \mathbf{r}')R(\mathbf{r}', t, \Delta t) \tag{10}$$

at a sufficiently large t where inelastic contributions in $R(\mathbf{r}, t, \Delta t)$ become negligible. From Eq. (10), the effective leading-order (LO) potential is obtained as

$$V^{\mathrm{LO}}_{\Delta t}(r) = \frac{\left[\frac{\nabla^2}{m_\pi} - \frac{\partial}{\partial t} + \frac{1}{4m_\pi}\frac{\partial^2}{\partial t^2}\right] R(\mathbf{r}, t, \Delta t)}{R(\mathbf{r}, t, \Delta t)}. \tag{11}$$

Using the rotational invariance of the potential, we can rewrite the above definition to improve signals as [24]

$$V^{\mathrm{LO}}_{\Delta t}(r) = \frac{\sum_{g\in O_h} R^\dagger(g\mathbf{r}, t, \Delta t)\left[\frac{\nabla^2}{m_\pi} - \frac{\partial}{\partial t} + \frac{1}{4m_\pi}\frac{\partial^2}{\partial t^2}\right] R(g\mathbf{r}, t, \Delta t)}{\sum_{g\in O_h} R^\dagger(g\mathbf{r}, t, \Delta t)R(g\mathbf{r}, t, \Delta t)}, \tag{12}$$

where O_h is the cubic rotation group. We also note that we employ the fourth-order difference approximation for ∇^2 to reduce discretization errors at short distances, since it turns out that physical observables in the deeply bound system are sensitive to the potential at short distances.

2.2. All-to-all propagator: the hybrid method

In this subsection we briefly explain the hybrid method, a technique for the all-to-all propagator calculation employed in this study. Let us consider the spectral decomposition of the quark propagator as

$$D^{-1}(x, y) = \sum_{i=0}^{N-1} \frac{1}{\lambda_i} v^{(i)}(x) \otimes v^{\dagger(i)}(y)\gamma_5, \tag{13}$$

where $v^{(i)}(x)$ and λ_i are eigenvectors and eigenvalues of the Hermitian Dirac operator $H = \gamma_5 D$, respectively, with N being the total number of eigenmodes, and color and spinor indices are implicit for simplicity. We assume here that $|\lambda_i| \leq |\lambda_j|$ for $i < j$.

The low-eigenmode approximation for the propagator with the spectral decomposition is introduced as

$$D_0^{-1}(x,y) = \sum_{i=0}^{N_{\rm eig}-1} \frac{1}{\lambda_i} v^{(i)}(x) \otimes v^{\dagger(i)}(y)\gamma_5, \qquad N_{\rm eig} < N, \tag{14}$$

while the remaining high-eigenmode part is estimated by using the Z_4 noise vector $\eta^{(i)}_{[r]}$, together with variance reduction by dilution as

$$D^{-1} - D_0^{-1} = H^{-1}\mathcal{P}_1\gamma_5 \approx \frac{1}{N_{\rm r}} \sum_{r=0}^{N_{\rm r}-1} \sum_{i=0}^{N_{\rm dil}-1} \psi^{(i)}_{[r]}(x) \otimes \eta^{\dagger(i)}_{[r]}(y)\gamma_5, \tag{15}$$

where $\mathcal{P}_1 \equiv \mathbf{1} - \sum_{i=0}^{N_{\rm eig}-1} v^{(i)} \otimes v^{\dagger(i)}$ is a projection onto the remaining high-eigenmode part, $N_{\rm r}$ ($N_{\rm dil}$) is a number of noise vectors (dilutions), and $\psi^{(i)}_{[r]}$ are solution vectors obtained by solving $H \cdot \psi^{(i)}_{[r]} = \mathcal{P}_1 \eta^{(i)}_{[r]}$. In this study, the temporal coordinate is diluted with the J-interlace as

$$\eta^{(i)}(\mathbf{x}, t) \neq 0 \text{ only if } t = i \bmod J. \tag{16}$$

For spatial coordinates, we introduce not only the $s2$ (even–odd) and $s4$ dilutions used in the previous study [21], but also an $s8$ dilution. In the $s8$ dilution, one noise vector is split into eight diluted vectors as

$$\begin{aligned}
\eta^{(0)} \neq 0 \quad &\text{if} \begin{cases} (n_x,n_y,n_z) = (\text{odd,odd,odd}) \text{ and } n_x+n_y+n_z = 1 \bmod 4, \\ (n_x,n_y,n_z) = (\text{even,even,even}) \text{ and } n_x+n_y+n_z = 2 \bmod 4; \end{cases} \\
\eta^{(1)} \neq 0 \quad &\text{if} \begin{cases} (n_x,n_y,n_z) = (\text{odd,odd,odd}) \text{ and } n_x+n_y+n_z = 3 \bmod 4, \\ (n_x,n_y,n_z) = (\text{even,even,even}) \text{ and } n_x+n_y+n_z = 0 \bmod 4; \end{cases} \\
\eta^{(2)} \neq 0 \quad &\text{if} \begin{cases} (n_x,n_y,n_z) = (\text{odd,even,even}) \text{ and } n_x+n_y+n_z = 1 \bmod 4, \\ (n_x,n_y,n_z) = (\text{even,odd,odd}) \text{ and } n_x+n_y+n_z = 2 \bmod 4; \end{cases} \\
\eta^{(3)} \neq 0 \quad &\text{if} \begin{cases} (n_x,n_y,n_z) = (\text{odd,even,even}) \text{ and } n_x+n_y+n_z = 3 \bmod 4, \\ (n_x,n_y,n_z) = (\text{even,odd,odd}) \text{ and } n_x+n_y+n_z = 0 \bmod 4; \end{cases} \\
\eta^{(4)} \neq 0 \quad &\text{if} \begin{cases} (n_x,n_y,n_z) = (\text{even,odd,even}) \text{ and } n_x+n_y+n_z = 1 \bmod 4, \\ (n_x,n_y,n_z) = (\text{odd,even,odd}) \text{ and } n_x+n_y+n_z = 2 \bmod 4; \end{cases} \\
\eta^{(5)} \neq 0 \quad &\text{if} \begin{cases} (n_x,n_y,n_z) = (\text{even,odd,even}) \text{ and } n_x+n_y+n_z = 3 \bmod 4, \\ (n_x,n_y,n_z) = (\text{odd,even,odd}) \text{ and } n_x+n_y+n_z = 0 \bmod 4; \end{cases} \\
\eta^{(6)} \neq 0 \quad &\text{if} \begin{cases} (n_x,n_y,n_z) = (\text{even,even,odd}) \text{ and } n_x+n_y+n_z = 1 \bmod 4, \\ (n_x,n_y,n_z) = (\text{odd,odd,even}) \text{ and } n_x+n_y+n_z = 2 \bmod 4; \end{cases} \\
\eta^{(7)} \neq 0 \quad &\text{if} \begin{cases} (n_x,n_y,n_z) = (\text{even,even,odd}) \text{ and } n_x+n_y+n_z = 3 \bmod 4, \\ (n_x,n_y,n_z) = (\text{odd,odd,even}) \text{ and } n_x+n_y+n_z = 0 \bmod 4. \end{cases}
\end{aligned} \tag{17}$$

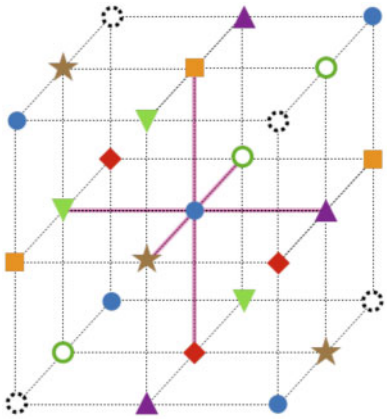

Fig. 1. Schematic representation of $s8$ space dilution. The different symbols indicate points which belong to different diluted vectors. The pink bands connect points used in the second-order approximation of the Laplacian at the central point.

See Fig. 1 for a schematic figure of the $s8$ dilution. Color and spinor indices are fully diluted in this study.

Combining the low-eigenmode and high-eigenmode parts, the all-to-all propagator is written as

$$D^{-1} \approx \frac{1}{N_{\rm r}} \sum_{r=0}^{N_{\rm r}-1} \sum_{i=0}^{N_{\rm hl}-1} u_{[r]}^{(i)} \otimes w_{[r]}^{\dagger(i)} \gamma_5, \tag{18}$$

where the hybrid lists $u_{[r]}^{(i)}, w_{[r]}^{(i)}$ are defined by

$$w_{[r]}^{(i)} = \left\{ \frac{v^{(0)}}{\lambda_0}, \ldots, \frac{v^{(N_{\rm eig}-1)}}{\lambda_{N_{\rm eig}-1}}, \eta_{[r]}^{(0)}, \ldots, \eta_{[r]}^{(N_{\rm dil}-1)} \right\}, \tag{19}$$

$$u_{[r]}^{(i)} = \left\{ v^{(0)}, \ldots, v^{(N_{\rm eig}-1)}, \psi_{[r]}^{(0)}, \ldots, \psi_{[r]}^{(N_{\rm dil}-1)} \right\}, \tag{20}$$

with $N_{\rm hl} = N_{\rm eig} + N_{\rm dil}$.

2.3. *Correlation function with the hybrid method*

The correlation function $F(\mathbf{r}, t, \Delta t)$ with the ρ-type source operator,

$$F(\mathbf{r}, t, \Delta t) = \sum_{\mathbf{y}, t_0} \langle (\pi\pi)_{I=1, I_z=0}(\mathbf{r}, t + t_0, \Delta t) \bar{\rho}_3^0(\mathbf{y}, t_0) \rangle, \tag{21}$$

is expressed in terms of the hybrid method (up to an overall sign) as

$$\begin{aligned} &\sum_{i,j,k} \sum_{\mathbf{x}, t_0} O_{[r,s]}^{(i,j)}(\mathbf{r} + \mathbf{x}, t + t_0 + \Delta t) O_{3[s,p]}^{(j,k)}(t_0) O_{[p,r]}^{(k,i)}(\mathbf{x}, t + t_0) \\ &\quad - O_{[r,s]}^{(i,j)}(\mathbf{x}, t + t_0) O_{3[s,p]}^{(j,k)}(t_0) O_{[p,r]}^{(k,i)}(\mathbf{r} + \mathbf{x}, t + t_0 + \Delta t), \end{aligned} \tag{22}$$

where

$$O_{3[r,s]}^{(i,j)}(t) \equiv \sum_{\mathbf{x}} w_{[r]}^{\dagger(i)}(\mathbf{x}, t) \gamma_5 \gamma_3 u_{[s]}^{(j)}(\mathbf{x}, t), \qquad O_{[r,s]}^{(i,j)}(\mathbf{x}, t) \equiv w_{[r]}^{\dagger(i)}(\mathbf{x}, t) u_{[s]}^{(j)}(\mathbf{x}, t). \tag{23}$$

Note that equal-time quark propagators would appear due to contractions in the sink operator if we took $\Delta t = 0$ in the calculation.

Table 1. Numerical setup for the calculations.

	Source	Scheme	N_{conf}	Stat. error
Case 0	Point	Equal time ($\Delta t = 0$)	20	Jackknife with bin size 1
Case 1a	Smear	Different time ($\Delta t = 1$)	20	Jackknife with bin size 1
Case 1b	Smear	Different time ($\Delta t = 1$)	60	Jackknife with bin size 6

Table 2. Setups for the hybrid method in our calculation. N_{eig} is the number of low eigenmodes for the all-to-all propagator. Color and spinor dilutions are always used.

	Time dilution	Space dilution	N_{eig}
Case 0	16-interlace	$s2$	100
Case 1a, 1b (src-to-sink)	16-interlace	$s4$	100
Case 1a, 1b (sink-to-sink)	4-interlace	$s8 \times s2$	100

3. Simulation details

In this study we employ $(2 + 1)$-flavor full QCD configurations generated by the JLQCD and CP-PACS Collaborations [25] on a $16^3 \times 32$ lattice with the Iwasaki gauge action [26] at $\beta = 1.83$ and a non-perturbatively improved Wilson–Clover action [27] at $c_{SW} = 1.7610$ and hopping parameters $(\kappa_{ud}, \kappa_s) = (0.1376, 0.1371)$. These parameters correspond to a lattice spacing of $a = 0.1214$ fm, a pion mass of $m_\pi \approx 870$ MeV, and a ρ meson mass of $m_\rho \approx 1230$ MeV. Note that the ρ meson is not a resonance but a bound state of two pions in this calculation. The periodic boundary condition is employed for all spacetime directions.

Table 1 shows the details of our numerical setup, and the parameters for the hybrid method are summarized in Table 2. In case 0, the source operator in Eq. (9) is constructed from the point quark source. In cases 1a and 1b, on the other hand, we employ the smeared quark source $q_s(\mathbf{x}, t) = \sum_{\mathbf{y}} f(\mathbf{x} - \mathbf{y}) q(\mathbf{y}, t)$ with the Coulomb gauge fixing, so that inelastic contributions are reduced at earlier imaginary times. The smearing function f is given by [29]

$$f(\mathbf{x}) = \begin{cases} a e^{-b|\mathbf{x}|} & (0 < |\mathbf{x}| < (L-1)/2), \\ 1 & (|\mathbf{x}| = 0), \\ 0 & (|\mathbf{x}| \geq (L-1)/2), \end{cases} \tag{24}$$

with $a = 1.0$, $b = 0.47$ in lattice units. As regards the setup for the random noise vectors, case 0 is calculated with three independent Z_4 noise vectors corresponding to r, s, p in Eq. (22). In cases 1a and 1b, we generate four different sets of three Z_4 noise vectors, and take an average over $4 \times 3! = 24$ samples ($3! = 6$ samples for each set using the permutation of r, s, p) to reduce noise contamination.

In case 0, we employ the equal-time ($\Delta t = 0$) scheme. As will be shown in Sect. 4.1, however, the statistical errors of the potential are found to be too large to obtain physical results, probably due to the statistical fluctuations associated with the stochastic estimations of equal-time quark propagation in the sink operator. In order to handle this problem, we employ the different-time ($\Delta t = 1$) scheme in cases 1a and 1b. Compared to the equal-time scheme, noise associated with the sink-to-sink quark propagator with zero space-time propagation distance are absent, and thus the statistical fluctuations are expected to be milder. In cases 1a and 1b, we also make spatial dilutions finer to further suppress

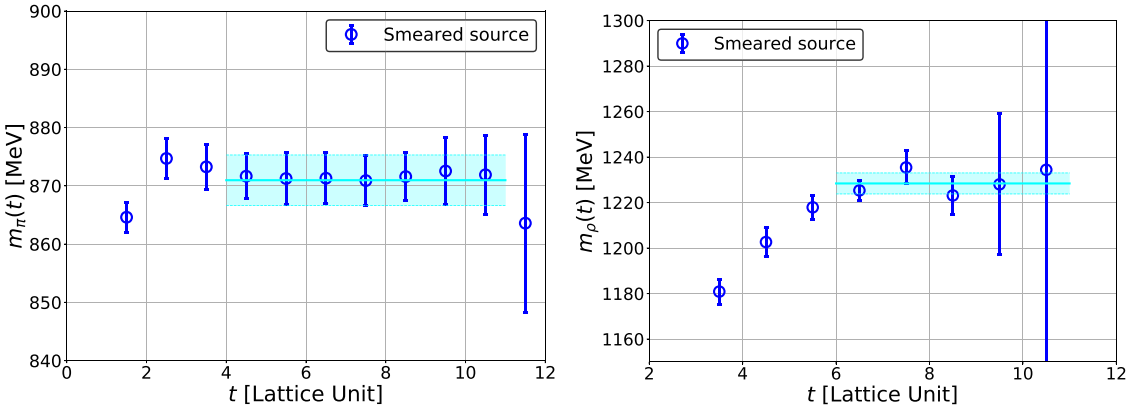

Fig. 2. (Left) The effective mass of the pion. (Right) The effective mass of the ρ meson. Both effective masses are obtained in case 1b. Each cyan solid line with band indicates the central value and its statistical error obtained from the fit to the corresponding correlation function within this interval.

noise contaminations. Namely, we employ $s8 \times s2$ and $s4$ dilutions for the sink-to-sink and source-to-sink propagators, respectively, as opposed to $s2$ dilutions in case 0. The increased numerical costs are partly compensated by decreasing the temporal dilution for the sink-to-sink propagators from 16-interlace to 4-interlace. Since we found in the previous study [21] that propagations along the temporal direction from t_0 to t_0+t with $t < J/2$ are not distorted much by the J-interlace dilution, the 4-interlace temporal dilution reduces the computational cost for sink-to-sink propagations without additional strong noise enhancements. We employ the same number of configurations for cases 0 and 1a, in order to verify the effect of the noise reductions. We increase the statistics of case 1a to 60 configurations in case 1b for measurements of physical quantities. The statistical errors are estimated by the jackknife method with bin size 1 (6) in case 0 and case 1a (case 1b).

Figure 2 shows the effective masses (with a half-integer time convention [21]) obtained in case 1b for pion $m_\pi(t)$ and ρ meson $m_\rho(t)$, which are calculated from $C(t)$ and $F(t) \equiv \sum_{\mathbf{r}} \bar{Y}_{l=1,m=0}(\Omega_{\mathbf{r}})F(\mathbf{r},t,\Delta t)$, respectively. Note that we insert the spherical harmonics for the P-wave $\bar{Y}_{l=1,m=0}$ in the summation to obtain $F(t)$, which is relevant to the ρ meson. The fit to $C(t)$ at $t = 4$–11 gives $m_\pi = 871(4)$ MeV, while the fit to $F(t)$ at $t = 6$–11 gives $m_\rho = 1228(5)$ MeV. The ratio of m_π to m_ρ becomes $m_\pi/m_\rho = 0.709(4)$, which is consistent with $m_\pi/m_\rho = 0.7076(18)$ as reported in the previous study [25]. Figure 2 also shows that the ground state saturations in $C(t)$ and $F(t)$ are achieved at least $t = 4$ and $t = 6$, respectively, in case 1b. In case 0, while the ground state saturation in $C(t)$ is achieved at a later time than case 1b (see Fig. 2 (left) in Ref. [21]), $t = 6$ is found to be sufficient since the errors in the potential are dominated by the statistical fluctuations, as will be shown in Sect. 4.1. In the following, we take the results at $t = 6$ as our central values and use the results at $t = 5, 7$ to estimate the systematic errors associated with their time dependence.

4. Results

4.1. Potential in case 0

We first consider case 0 for the $I = 1$ $\pi\pi$ potential, whose setup for the hybrid method is the same as case 3 for the $I = 2$ $\pi\pi$ potential in Ref. [21]. In the previous study, we found that the $I = 2$ $\pi\pi$ potential is reasonably accurate at $t < 8$. Figure 3 (left) shows the potential obtained at $t = 6$. As can be seen, the potential has extremely large statistical fluctuations in this setup. Since equal-time quark propagations at the sink were absent for the $I = 2$ $\pi\pi$ potential in the previous study, we

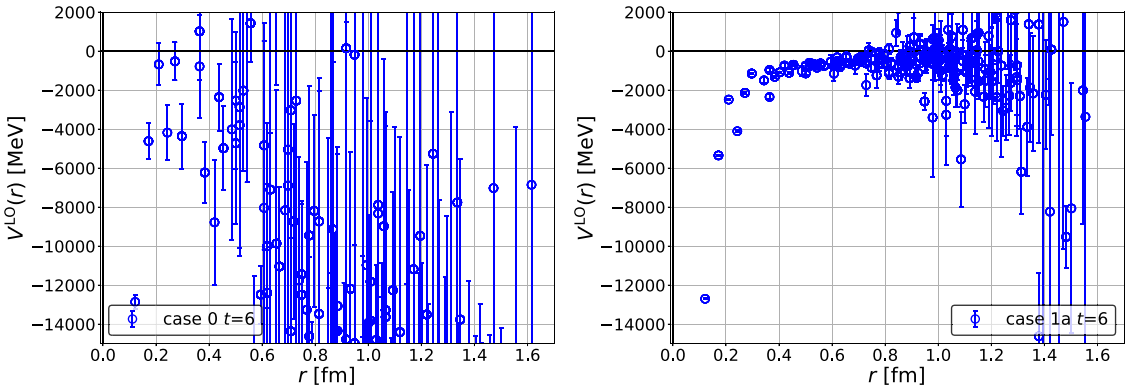

Fig. 3. (Left) The potential at $t = 6$ in case 0 (the same setup as case 3 in Ref. [21]). (Right) The potential at $t = 6$ in case 1a.

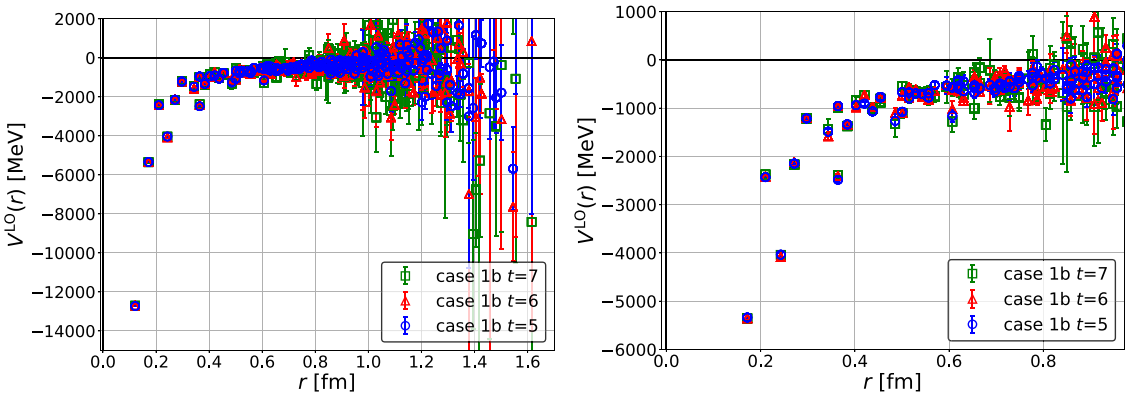

Fig. 4. Time dependence of the potential in case 1b. (Left) Overall view. (Right) Enlarged view at $r \leq L/2$.

suspect that extremely large statistical fluctuations for the $I = 1$ $\pi\pi$ potential are caused by noise contaminations from the hybrid method to evaluate such equal-time propagations at the sink.

To suppress such noise contamination, we additionally employ three noise reduction techniques: (1) the different-time scheme for the NBS wave function to avoid the equal-time propagation, (2) finer space dilution in the quark annihilation part (as well as in the valence quark part) to reduce noise contamination in spatial indices, (3) the average over the increased number of noise vectors. In the following, we will show the results in cases 1a and 1b with these three improvements, whose details were already explained in Sect. 3.

4.2. Potential with additional noise reductions in case 1

The potential in case 1a at $t = 6$ is shown in Fig. 3 (right). Since the smeared quark sources are employed in case 1a, $t = 6$ is large enough to suppress elastic contributions to the potential. Thanks to the three additional noise reduction techniques mentioned in Sect. 4.1, the statistical fluctuations of the potential are drastically reduced. In this study, we do not clarify which noise reduction technique is the most important, since some additional calculations (for example, calculations using only one of the three noise reduction techniques) are required for this purpose. We instead focus on increasing the statistics with the same setup as case 1a, which is labeled as case 1b and whose results are shown in Fig. 4.

Table 3. Resultant fitting parameters and χ^2/d.o.f. at $t = 6$. All values are in lattice units.

a_0	a_1	a_2	a_3	a_4	a_5	χ^2/d.o.f.
−1.7(0.2)	2.0(0.1)	−0.64(0.04)	6.5(0.2)	−21.0(0.1)	0.886(0.008)	7.59

The potential shows a strong attraction without a repulsive core, which is consistent with the existence of the deeply bound ρ meson in this system. As shown in Fig. 4, the potential is almost independent of time at $t = 5, 6, 7$, as expected from the effective energy shown in Fig. 2. Interestingly, we notice that statistical fluctuations of the potential increase as the distance r increases. We interpret this behavior qualitatively as follows. Two-pion scattering states give dominant contributions to the long-distance part of the potential, as the two-pion sink operator in the NBS wave function at large r strongly couples to them. The bound ρ meson state, on the other hand, gives large contributions to the short-distance part of the potential. Since the ρ-type operator we employ at the source rarely creates such two-pion scattering states, it is hard to determine the long-distance part of the potential precisely, and thus the statistical fluctuations become large. We also observe that the short-distance part of the potential has non-smooth behaviors, which probably come from higher partial wave contaminations, for example the $l = 3$ partial wave in our case, as similar behaviors have sometimes been observed for the HAL QCD potentials in previous studies, and rotational breaking by the discretization artifact is expected to be enhanced at short distance.

To calculate physical observables such as binding energies and scattering phase shifts, we fit the potential on discrete lattice points by a sum of three Gauss functions given by

$$V(r) = a_0 e^{-(r/a_1)^2} + a_2 e^{-(r/a_3)^2} + a_4 e^{-(r/a_5)^2}. \tag{25}$$

Several issues for the fit of the potential are seen here. The first one is the finite-volume effect. As seen in Fig. 3 (right), the potential deviates from zero even at $r = La/2 = 0.9712$ fm due to the finite-volume effect of the periodic boundary condition. We therefore partly include this finite-volume effect into the fit as

$$V(\mathbf{r})_{\mathrm{PBC}} = V(\mathbf{r}) + \sum_{\mathbf{n}\in\{(0,0,\pm1),(0,\pm1,0),(\pm1,0,0)\}} V(\mathbf{r} + L\mathbf{n}). \tag{26}$$

The second issue is the non-smooth behavior of the potential at short distance, as mentioned before. To make the fit stable, we have to exclude two points of the potential, at $r = 0.2428$ and 0.3642 fm, which deviate considerably from the other data points. We expect that the exclusion of these points partly reduces the systematic uncertainty associated with the contaminations from higher partial waves at short distances. We leave a more detailed analysis for future investigations with finer lattices and a new partial wave decomposition method [28]. Table 3 gives the result of the fit at $t = 6$, and Fig. 5 shows the original potential and the fitting result. Note that χ^2/d.o.f. = 7.59 is much larger than 1, even with the exclusion of the two data points at $r = 0.2428$ and 0.3642 fm in the fit, since the remaining data points at short distance still have scattered central values with small statistical errors.

4.3. Physical observables

Using the potential given by Eq. (25), we calculate the ground state energy of the $I = 1$ $\pi\pi$ system in infinite volume. We employ the Gaussian expansion method (GEM) [30] to evaluate the ground

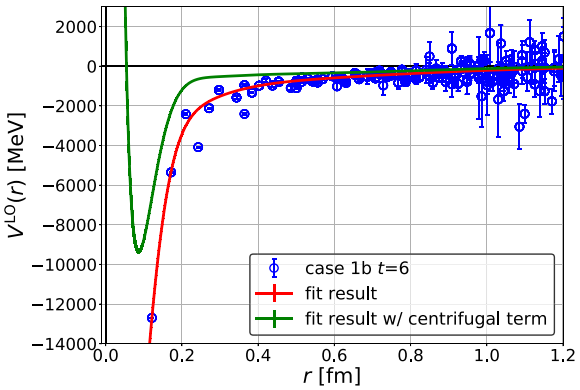

Fig. 5. Fitting result at $t = 6$. The blue points are the original data, and the red line shows the fitting result. The green line is the fitting result curve with the centrifugal potential term with $l = 1$, $V_c(r) = \frac{1}{m_\pi}\frac{1\cdot 2}{r^2}$.

state energy, which is given by

$$E_{\text{bind}} = 668 \pm 24_{\text{stat}} \begin{pmatrix} +69 \\ -151 \end{pmatrix}_{\text{sys(time dep.)}} \text{MeV}, \tag{27}$$

where the first error denotes the statistical error and the second error the systematic one estimated by the time dependence of the binding energy at $t = 6 \pm 1$. Comparing with the binding energy $E_{\text{bind}} = |m_\rho - 2m_\pi| \approx 515\,\text{MeV}$ from m_π and m_ρ (see Sect. 3), the results are consistent with each other within a large systematic error in Eq. (27).

We also remark on the systematic error associated with the fit of the potential. As mentioned in the previous subsection, some unreliable points have to be excluded in the fit, and the data points at short distances are still scattered with small statistical errors, which leads to large χ^2/d.o.f. In such a situation, the fit for the short-range part as well as the resultant binding energy may have additional large uncertainty, since the latter is rather sensitive to the structure of the potential at short distances. While the corresponding systematic error is not fully quoted in Eq. (27), part of such systematics seems to be reflected in the systematic error estimated from the time dependence. In fact, we find that the time dependence of the results is substantial even though the potential is rather time independent, as shown in Fig. 4. This indicates that the large time dependence mostly originates from the uncertainty in the fit of the potential. To make the systematic uncertainties fully under control, we need to employ calculations at finer lattice spacings to obtain more data points at short distances or to find a better scheme for the NBS wave function to have smoother behaviors at short distances. Having noted the above open issue, we can still positively conclude that it is possible to calculate reasonably precise potentials in systems including quark creation/annihilation processes by a combination of the hybrid method and the HAL QCD method.

We finally discuss the relation between $k^3 \cot\delta_1(k)$ and the bound state pole in detail, as the normality check proposed in Ref. [29]. In the P-wave scattering, $k^3 \cot\delta_1(k)$ is related to the scattering S-matrix $S_1(k)$ as

$$k^3 \cot\delta_1(k) = ik^3 \frac{S_1(k)+1}{S_1(k)-1}. \tag{28}$$

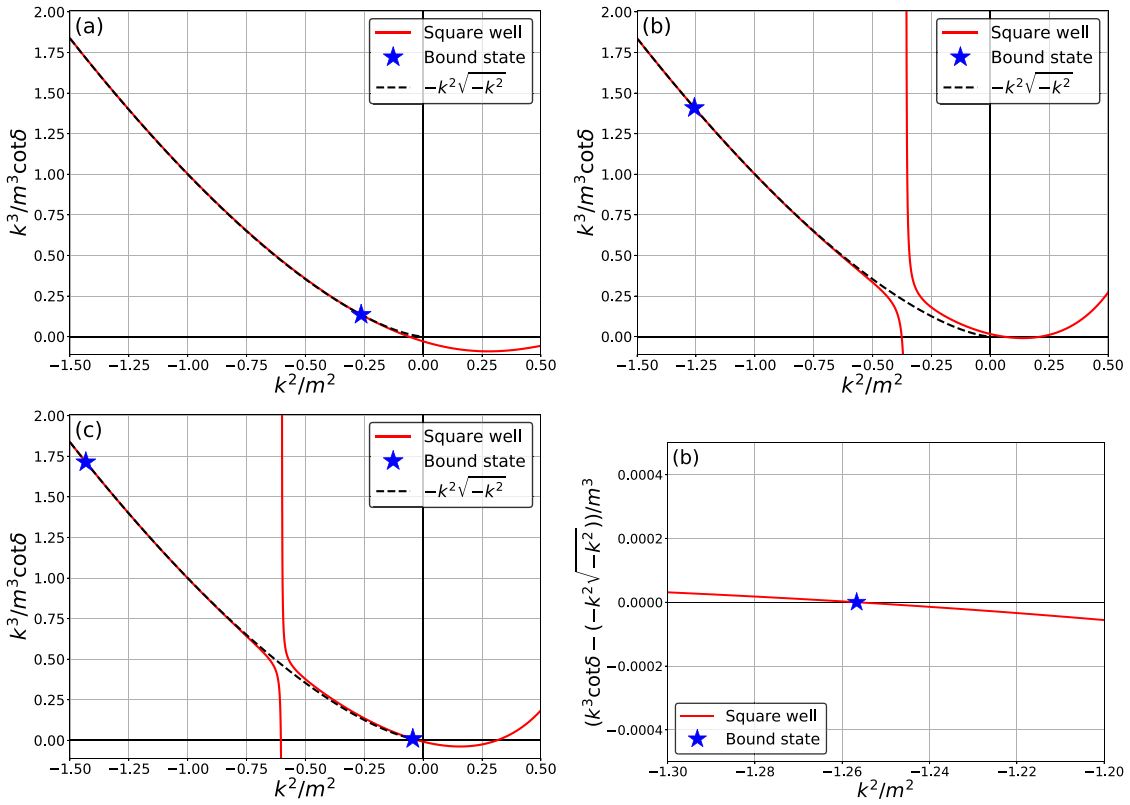

Fig. 6. Typical behavior of $k^3\cot\delta_1$ in the P-wave calculated with the square well potential, together with the bound state condition (black dashed line) and pole of bound states (blue star). (a) Shallowly bound case (weak attraction). (b) Deeply bound case (strong attraction). The second branch can be seen on the right-hand side. A difference between $k^3\cot\delta_1(k)$ and $-k^2\sqrt{-k^2}$ around the bound state pole is also shown on the lower right side. (c) Doubly bound case (very strong attraction). The second branch reaches the bound state condition and the second bound state emerges.

Generally, the scattering S-matrix in P-wave near the bound state pole ($k \approx i\kappa_b$) behaves as [31]

$$S_1(k) \approx \frac{i\beta_b^2}{k - i\kappa_b}, \tag{29}$$

where κ_b is the absolute value of k for the pole and β_b^2 is a positive real constant related to the normalization factor of the wave function of the bound state. By using Eqs. (28) and (29), the physical pole condition in P-wave becomes

$$\frac{d}{dk^2}\left[k^3\cot\delta_1(k) - (-k^2\sqrt{-k^2})\right]\Big|_{k^2=-\kappa_b^2} = -\frac{\kappa_b^2}{\beta_b^2} < 0. \tag{30}$$

In Fig. 6, we show typical behaviors of $k^3\cot\delta_1(k)$ calculated by the square well potential in several cases. We can see how $k^3\cot\delta_1(k)$ evolves when the attraction becomes stronger from Fig. 6(a)–(c). As seen in Fig. 6(b), the deeply bound state appears as the intersection (blue solid star) between $-k^2\sqrt{-k^2}$ (the bound state condition, black dashed line) and a branch of $k^3\cot\delta_1(k)$ (red solid line) disconnected from a branch at the origin ($k^2 = 0$). Moreover, $k^3\cot\delta_1(k)$ satisfies the physical pole condition, Eq. (30) [see Fig. 6(b) (lower right)].

These two typical behaviors of $k^3\cot\delta_1$ in the presence of one deeply bound state in the P-wave are indeed observed for our data obtained from the potential at $t = 6$: Fig 7 (left) shows

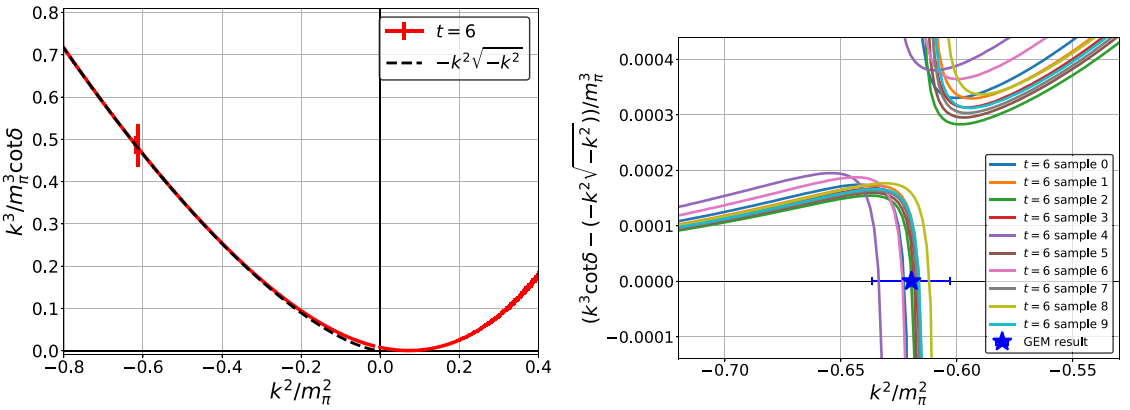

Fig. 7. (Left) $k^3 \cot\delta_1(k)$ (red solid lines) calculated with the potential at $t = 6$, together with the bound state condition (black dashed line). Note that the red solid lines diverge to $\pm\infty$ around $k^2/m_\pi^2 \approx -0.6$. (Right) A difference between $k^3 \cot\delta_1(k)$ and $-k^2\sqrt{-k^2}$ around the intersection for each jackknife sample, together with k^2 corresponding to the binding energy obtained by the Gaussian expansion method (blue solid star). It can be seen that all samples satisfy the physical pole condition and have a discontinuity, which typically appears for a deeply bound system.

that an intersection between $-k^2\sqrt{-k^2}$ (black dashed line) and $k^3 \cot\delta_1(k)$ (red solid line) in the branch disconnected from the origin appears at $k^2/m_\pi^2 \approx -0.623$, corresponding to the GEM result, $E_{\rm bind} \approx 668$ MeV. Shown in Fig. 7 (right) is $(k^3 \cot\delta_1(k) - (-k^2\sqrt{-k^2}))/m_\pi^3$ for each jackknife sample, and we confirm that the physical pole condition is satisfied for all samples.

5. Summary and outlook

We have calculated the HAL QCD potential of the $I = 1\,\pi\pi$ system at $(m_\pi, m_\rho) \approx (870, 1230)$ MeV, using the hybrid method for all-to-all propagators. While statistical fluctuations in the straightforward calculation are found to be extremely large due to the quark creation/annihilation process, we have successfully obtained the precise potential by developing various noise reduction techniques such as space dilutions and the non-equal time scheme for the potential. We have calculated physical quantities such as the binding energy and phase shifts from the potential. It is observed that our potential reproduces the characteristic features of the deeply bound ρ meson, whose binding energy is consistent with that obtained from the temporal correlation within a large systematic error in the former. The large systematic error in the present calculations is caused by the uncertainty of the fit for the potential at short distances, whose origin is attributed to contamination from higher partial wave components.

Finally, we would like to comment on further improvements to our calculation in the future. This and previous studies [21] on the hybrid method reveal that one can obtain reasonably precise potentials as long as appropriate setups for calculations are introduced, but on the other hand, it is also found that the numerical cost for noise reduction seems too large to perform such calculations on larger lattice volumes. Therefore, we have to investigate possibilities to achieve both small noise contamination and small numerical costs. Fortunately, we find that a combination of some other techniques such as all-mode averaging [32], the one-end trick, and sequential propagators [33] is promising to achieve the above requirements. As a first step toward this direction, we are now working on the ρ resonance at $m_\pi \approx 410$ MeV with new improved methods, and results will be reported in the near future.

Acknowledgements

The authors thank members of the HAL QCD Collaboration for fruitful discussions. We thank the JLQCD and CP-PACS Collaborations [25] and ILDG/JLDG (http://www.lqcd.org/ildg, http://www.jldg.org) [35] for providing their configurations. All of the simulations were performed on the HOKUSAI Big-Waterfall in RIKEN. The framework of our numerical code is based on the Bridge++ codeset (http://bridge.kek.jp/Lattice-code/) [34]. Y. A. is supported in part by the Japan Society for the Promotion of Science (JSPS). This work is supported in part by Grants-in-Aid of the Japanese Ministry of Education, Sciences and Technology, Sports and Culture (MEXT) for Scientific Research (Nos. JP16H03978, JP18H05236, JP18H05407, JP19K03879), by a priority issue (Elucidation of the fundamental laws and evolution of the universe) to be tackled by using Post "K" Computer, and by Joint Institute for Computational Fundamental Science (JICFuS).

Funding

Open Access funding: SCOAP[3].

References

[1] M. Lüscher, Nucl. Phys. B **354**, 531 (1991).
[2] K. Rummukainen and S. Gottlieb, Nucl. Phys. B **450**, 397 (1995) [arXiv:hep-lat/9503028] [Search INSPIRE].
[3] M. T. Hansen and S. R. Sharpe, Phys. Rev. D **86**, 016007 (2012) [arXiv:1204.0826 [hep-lat]] [Search INSPIRE].
[4] N. Ishii, S. Aoki, and T. Hatsuda, Phys. Rev. Lett. **99**, 022001 (2007) [arXiv:nucl-th/0611096] [Search INSPIRE].
[5] S. Aoki, T. Hatsuda, and N. Ishii, Prog. Theor. Phys. **123**, 89 (2010) [arXiv:0909.5585 [hep-lat]] [Search INSPIRE].
[6] S. Aoki [HAL QCD Collaboration], Prog. Part. Nucl. Phys. **66**, 687 (2011) [arXiv:1107.1284 [hep-lat]] [Search INSPIRE].
[7] N. Ishii et al. [HAL QCD Collaboration], Phys. Lett. B **712**, 437 (2012) [arXiv:1203.3642 [hep-lat]] [Search INSPIRE].
[8] R. A. Briceño, J. J. Dudek, and R. D. Young, Rev. Mod. Phys. **90**, 025001 (2018) [arXiv:1706.06223 [hep-lat]] [Search INSPIRE].
[9] M. Werner et al., Eur. Phys. J. A **56**, 61 (2020) [arXiv:1907.01237 [hep-lat]] [Search INSPIRE].
[10] C. Alexandrou, L. Leskovec, S. Meinel, J. Negele, S. Paul, M. Petschlies, A. Pochinsky, G. Rendon, and S. Syritsyn, Phys. Rev. D **96**, 034525 (2017) [arXiv:1704.05439 [hep-lat]] [Search INSPIRE].
[11] S. Aoki, N. Ishii, T. Doi, T. Hatsuda, Y. Ikeda, T. Inoue, K. Murano, H. Nemura, K. Sasaki [HAL QCD Collaboration], Proc. Japan Acad. B **87**, 509 (2011) [arXiv:1106.2281 [hep-lat]] [Search INSPIRE].
[12] T. Iritani, S. Aoki, T. Doi, T. Hatsuda, Y. Ikeda, T. Inoue, N. Ishii, H. Nemura and K. Sasaki [HAL QCD Collaboration], J. High Energy Phys. **1903**, 007 (2019) [arXiv:1812.08539 [hep-lat]] [Search INSPIRE].
[13] Y. Ikeda, S. Aoki, T. Doi, S. Gongyo, T. Hatsuda, T. Inoue, T. Iritani, N. Ishii, K. Murano, and K. Sasaki [HAL QCD Collaboration], Phys. Rev. Lett. **117**, 242001 (2016) [arXiv:1602.03465 [hep-lat]] [Search INSPIRE].
[14] Y. Ikeda [HAL QCD Collaboration], J. Phys. G: Nucl. Part. Phys. **45**, 024002 (2018) [arXiv:1706.07300 [hep-lat]] [Search INSPIRE].
[15] S. Gongyo et al., Phys. Rev. Lett. **120**, 212001 (2018) [arXiv:1709.00654 [hep-lat]] [Search INSPIRE].
[16] T. Iritani et al., Phys. Lett. B **792**, 284 (2019) [arXiv:1810.03416 [hep-lat]] [Search INSPIRE].
[17] D. Kawai, S. Aoki, T. Doi, Y. Ikeda, T. Inoue, T. Iritani, N. Ishii, T. Miyamoto, H. Nemura, K. Sasaki [HAL QCD Collaboration], Prog. Theor. Exp. Phys. **2018**, 043B04 (2018) [arXiv:1711.01883 [hep-lat]] [Search INSPIRE].
[18] D. Kawai [HAL QCD Collaboration], EPJ Web Conf. **175**, 05007 (2018).
[19] M. Peardon, J. Bulava, J. Foley, C. Morningstar, J. Dudek, R. G. Edwards, B. Joó, H.-W. Lin, D. G. Richards, and K. J. Juge [Hadron Spectrum Collaboration], Phys. Rev. D **80**, 054506 (2009) [arXiv:0905.2160 [hep-lat]] [Search INSPIRE].
[20] J. Foley, K. Jimmy Juge, A. Ó Cais, M. Peardon, S. M. Ryan, and J.-I. Skullerud [TrinLat Collaboration], Comput. Phys. Commun. **172**, 145 (2005) [arXiv:hep-lat/0505023] [Search INSPIRE].

[21] Y. Akahoshi, S. Aoki, T. Aoyama, T. Doi, T. Miyamoto, and K. Sasaki, Prog. Theor. Exp. Phys. **2019**, 083B02 (2019) [arXiv:1904.09549 [hep-lat]] [Search INSPIRE].
[22] S. Aoki, T. Doi, T. Hatsuda, Y. Ikeda, T. Inoue, N. Ishii, K. Murano, H. Nemura, K. Sasaki [HAL QCD Collaboration], Prog. Theor. Exp. Phys. **2012**, 01A105 (2012) [arXiv:1206.5088 [hep-lat]] [Search INSPIRE].
[23] S. Aoki, N. Ishii, T. Doi, Y. Ikeda, and T. Inoue, Phys. Rev. D **88**, 014036 (2013) [arXiv:1303.2210 [hep-lat]] [Search INSPIRE].
[24] K. Murano, N. Ishii, S. Aoki, T. Doi, T. Hatsuda, Y. Ikeda, T. Inoue, H. Nemura, and K. Sasaki [HAL QCD Collaboration], Phys. Lett. B **735**, 19 (2014) [arXiv:1305.2293 [hep-lat]] [Search INSPIRE].
[25] T. Ishikawa et al. [CP-PACS and JLQCD Collaborations], Phys. Rev. D **78**, 011502(R) (2008) [arXiv:0704.1937 [hep-lat]] [Search INSPIRE].
[26] Y. Iwasaki, Nucl. Phys. B **258**, 141 (1985).
[27] B. Sheikholeslami and R. Wohlert, Nucl. Phys. B **259**, 572 (1985).
[28] T. Miyamoto, Y. Akahoshi, S. Aoki, T. Aoyama, T. Doi, S. Gongyo, and K. Sasaki, Phys. Rev. D **101**, 074514 (2020) [arXiv:1906.01987 [hep-lat]] [Search INSPIRE].
[29] T. Iritani, S. Aoki, T. Doi, T. Hatsuda, Y. Ikeda, T. Inoue, N. Ishii, H. Nemura, and K. Sasaki [HAL QCD Collaboration], Phys. Rev. D **96**, 034521 (2017) [arXiv:1703.07210 [hep-lat]] [Search INSPIRE].
[30] E. Hiyama, Y. Kino, and M. Kamimura, Prog. Part. Nucl. Phys. **51**, 223 (2003).
[31] A. G. Sitenko, *Scattering Theory* (Springer, Berlin, 1991).
[32] E. Shintani, R. Arthur, T. Blum, T. Izubuchi, C. Jung, and C. Lehner, Phys. Rev. D **91**, 114511 (2015) [arXiv:1402.0244 [hep-lat]] [Search INSPIRE].
[33] A. Abdel-Rehim, C. Alexandrou, J. Berlin, M. Dalla Brida, J. Finkenrath, and M. Wagner, Comput. Phys. Commun. **220**, 97 (2017) [arXiv:1701.07228 [hep-lat]] [Search INSPIRE].
[34] S. Ueda, S. Aoki, T. Aoyama, K. Kanaya, H. Matsufuru, S. Motoki, Y. Namekawa, H. Nemura, Y. Taniguchi, and N. Ukita, J. Phys. Conf. Ser. **523**, 012046 (2014).
[35] T. Amagasa et al., J. Phys. Conf. Ser. **664**, 042058 (2015).